Multi-mechanism theory of aerosol capture by fibrous filters, including fiber diameter/orientation dispersity and particle morphology effects. Preliminary tests vs. data for mobility-selected submicron particles

Daniel E. Rosner*

Chemical and Environmental Engineering Dept. Yale University, Mason Laboratory, 9 Hillhouse Ave., New Haven, CT 06520-8286, USA

Manuel Arias-Zugasti

Departamento de Física Matemática y de Fluidos, Universidad Nacional de Educación a Distancia (UNED), Av. de Esparta s/n, Las Rozas (Madrid) 28232, Spain

Abstract

In Paper I (Sep. Purif. Technol. 257 (2021) 117676) we showed that a semi-analytic, multi-mechanism expression for the single-fiber capture fraction, $\eta_{\mathrm{cap,SF}}$, (derived using asymptotically valid approximations: $\mathrm{Re_f} < 0.4$, $\mathrm{Pe_f} \gg 1$, $R \ll 1$, $R \cdot \mathrm{Pe_f}^{1/3}$ arbitrary and $\mathrm{Stk_p} \leq \mathrm{Stk_{p_{crit}}}$), facilitates a deterministic-, pseudo-continuum aerosol population-balance (PB-) approach to predicting fibrous filter performance. There we explicitly considered "deep" ($L_\mathrm{f}/d_{\mathrm{f},g} \gg 1$), low solidity idealized fibrous filters (FFs) challenged by polydispersed aerosols—especially single-mode log-normal (LN) ASDs of modest spread captured by a spatially uniform array of fibers of a single diameter in crossflow. However, realistic fibrous filter media often possess a LN distribution of fiber diameters, as well as a near-Gaussian orientation distribution narrowly spread about normal incidence ($\theta = \pi/2$). Moreover, even if this were not so, there would be meso-scale departures from a uniform average fiber solid fraction. We show here that our tractable aerosol PBE-approach to idealized FF performance (Paper I) can be generalized to incorporate these particular structural features of commercially available fibrous filter media. But, to clarify whether these generalizations are likely to be useful, if not fully sufficient, for practical circumstances, it is also necessary to compare such methods/predictions against selected sets of well-defined experimental results. We initiate this program here, having chosen the recent experiments of Kang et al. (Sep. Purif. Technol. 209 (2019) 461–469) carried out using a commercially available fiberglass filter with $L_\mathrm{f}/d_{\mathrm{f},g} \simeq 300$, mean solid fraction of 0.039, and $d_{\mathrm{f},g} = 2.5$ μm, successively challenged by mobility-selected KCl(s) particles (with diameters between ca. 20 and 600 nm) at the carrier gas velocities of 15 and 10 cm/s—capture conditions dominated by the transport mechanism of Brownian diffusion and convection, with "interception" (associated with non-negligible $d_\mathrm{p}/d_\mathrm{f}$) becoming important above ca. $d_\mathrm{p} = 100$ nm. We conclude from these data that the effective *interception* diameter, $d_{\mathrm{p,icpt,eff}}$, of the particles studied is systematically larger than their stated *mobility* diameters—a situation which will deserve further attention in future studies. Encouraged by these preliminary but instructive comparisons, we expect that, for many current and future design purposes, our present class of semi-analytic/non-stochastic/multi-mechanism methods will provide a welcome complement, if not alternative, to much more computationally-intensive simulation methods for realistic fibrous media that have been described and implemented in the recent aerosol filtration literature. The consequences of including these structural features of fibrous filters in the presence of aerosol size- and shape polydispersity will be the subject of future studies, based on the generalized Population Balance Equation developed/proposed in Section 3.3.

Keywords: Fibrous filter aerosol capture theory, Aerosol deposition (multi-mechanism) on fibers, Fiber diam, orientation and mesoscale nonuniformity, Interception particle diam, Mobility particle diam, Sub-critical particle inertia effects on fibrous filter performance

1. Introduction and Motivation

The need to accurately accommodate not only multiple aerosol capture mechanisms (e.g., Brownian diffusion, interception, particle inertia) but also microstructural complexities of available fibrous filter media, has motivated many recent fibrous filter (FF) R&D studies—with an evident increasing reliance on 2D or even 3D numerical CFD computations combined with stochastic (e.g., Brownian Dynamics-) methods (see, e.g., Kang et al. (2019)). However, our recent demonstration that asymptotic tech-

*Corresponding author

Email addresses: daniel.rosner@yale.edu (Daniel E. Rosner), maz@dfmf.uned.es (Manuel Arias-Zugasti)

niques could be exploited to develop an accurate multi-mechanism, semi-analytic single fiber (SF-) capture fraction expression (see, e.g., Fernandez de la Mora & Rosner (2019) and Arias-Zugasti et al. (2019)) appears to facilitate an attractive alternative route to acceptable FF performance calculations—still based on the pseudo-continuum "single fiber efficiency" concept, as outlined and extended here. Our strategy is to exploit the quasi-separable functional form of our compact $\eta_{\mathrm{cap,SF}}$ expression to derive dimensionless "sensitivity coefficients", which will be shown to dramatically simplify the inclusion of often accessible microstructural information in FF-performance calculations, based on an aerosol population-balance approach for tracking the aerosol capture process. In the first part of this program, described more fully in Rosner & Arias-Zugasti (2021) (hereafter called Paper I) and briefly summarized in Section 2, attention was deliberately focused on a clean, idealized FF-medium in which all of the fibers were of one diameter and oriented normal to the carrier gas flow as well as being 'equi-spaced'. In Section 3 we show that the now-known sensitivity of $\eta_{\mathrm{cap,SF}}$ to small relative changes in fiber diameter and gas velocity, taken together with often available information on both fiber diameter- and fiber orientation- distribution functions, can be used to quantify the systematic effects of these two types of fiber 'dispersity' on aerosol size-dependent particle capture. We also introduce a plausible estimate for the unavoidable pdf of solid fraction in commercially available fibrous filter media—including its likely consequences for the expected 'pseudo-homogeneous' particle sink strength. Remarkably, our formally exact solution to the PBE based on the 'method of successive quadratures' (Paper I) will be shown to carry over to the present situation via the inclusion of three relevant particle-size dependent 'microstructure-sensitive' correction factors to the previously reported "ideal" FF/SF capture fraction.

However, before continuing down the path of examining instructive PBE-solutions for arbitrary-shaped feedborne ASDs a prudent first step would be to first test the accuracy of our suggested methods to estimate the nature/magnitude of these particular FF-micro-structure-induced effects. Toward this end, in the present paper (Sections 4, 5) we compare the predictions of our proposed approach vs. recent overall filter capture fraction measurements reported by Kang et al. (2019) for a commercially available fiberglass filter with $L_{\mathrm{f}}/d_{\mathrm{f},g} \simeq 300$ sequentially challenged with mobility-selected Ag(s) or KCl(s) particles ultimately between ca. 3 nm and 600 nm diameter.

These preliminary comparisons (Sections 4, 5), while necessary first steps, are sufficiently instructive and encouraging to provisionally recommend that our present methods could serve as a welcome complement, if not timely alternative, to much more 'computationally-intensive' alternative simulation methods for 'realistic' fibrous media described/implemented in the recent aerosol filtration literature.

2. PBE-Based Treatments of 'Idealized' FF Media Challenged by Polydispersed Aerosols

2.1. Fundamental single fiber (SF-) solution

For our first step on the path to a tractable, deterministic theory of FF performance, attention was focused on the isolated single cylindrical fiber multi-mechanism particle capture problem, but now including subcritical particle inertia and exploiting defensible asymptotic methods and conditions—including $\mathrm{Re} < 1$, flow normal to the cylinder axis, $\mathrm{Pe}^{1/3} \gg 1$, LBL-theory, $R \equiv d_{\mathrm{p}}/d_{\mathrm{f}} \ll 1$, $\mathrm{Stk} \leq \mathrm{Stk}_{\mathrm{crit}}$ and $\mathrm{Kn}_{\mathrm{f}} \ll 1$ (Fernandez de la Mora & Rosner (2019), Arias-Zugasti et al. (2019)). This led to the development of a factorable 'fundamental solution' for $\eta_{\mathrm{cap,SF}}$ of the instructive factorable form:

$$\eta_{\mathrm{cap,SF}} = f_0(\mathrm{Re}, \mathrm{Pe}, R) \cdot f_1(\Pi) \cdot E(S) \cdot F(\Pi, S) \qquad (1)$$

accounting fully for the interactive (*non*-additive) mechanisms of convective-diffusion, interception, and sub-critical particle inertia. Closed form results were provided for f_0 and f_1:

$$f_0(\mathrm{Re}, \mathrm{Pe}, R) = 2\pi \cdot [C(\mathrm{Re})]^{1/3} \cdot \mathrm{Pe}^{-2/3} \cdot (1+R)^{-1} \qquad (2)$$

and

$$f_1(\Pi) = Z(\Pi)/\Pi \qquad (3)$$

where:

$$Z(\Pi) = \frac{3^{2/3}\,\Pi\,\exp(-\Pi^3/6)}{2^{1/3}\,\Gamma(1/3, \Pi^3/6)} \qquad (4)$$

and where $\Pi = R \cdot [C(\mathrm{Re}) \cdot \mathrm{Pe}]^{1/3}$ is a modified Friedlander interception-diffusion parameter, which will therefore depend on R, Re and Pe. Here $C(\mathrm{Re}) \equiv \left[1 + \ln\left(\mathrm{Re}^{-1/2}\right)\right]^{-1}$ and, as seen in Eq. (4), $Z(\Pi)$ is expressible in terms of the incomplete gamma function, $\Gamma(1/3, \Pi^3/6)$ (Fernandez de la Mora & Rosner (2019)). The last two factors appearing in $\eta_{\mathrm{cap,SF}}$, written $E(S)$ and $F(\Pi, S)$ in Eq.(1), required numerical integrations, i.e. the stagnation region external "inertial enrichment" factor: $E(S)$, and the recently computed universal bi-variate function: $F(\Pi, S)$, obtained via a linear parabolic PDE to find the particle fluxes across the thin mass transfer boundary layer that develops in the gas phase "hugging" the effective fiber surface (one particle radius away from the actual solid surface.) Tabular values were provided for both $E(S)$ and $F(\Pi, S)$ in Arias-Zugasti et al. (2019) in the range $0 \leq S \leq S_{\mathrm{crit}}$, (with E behaving like $\exp(1.8941S)$ for small S and S_{crit} found to be 2.2145) and, for the interception-diffusion parameter: Π ($0 \leq \Pi \leq \infty$). To avoid the need for frequent bivariate interpolations, the following accurate correlation (error < ca. 2 pct) for the resulting $F(\Pi, S)$-values was provided:

$$F(\Pi, S) \simeq [F(0, S)]^{m(\Pi)} \cdot [F(\infty, S)]^{1-m(\Pi)} \qquad (5)$$

where the limiting functions $F(0,S) = F_0(S)$ and $F(\infty,S) = F_\infty(S)$ were reported (Fernandez de la Mora & Rosner (2019)) and:

$$m(\Pi) \simeq \left(1 + 0.4\Pi^{5/3}\right)^{-1} \tag{6}$$

A short table of $E(S)$, $F_0(S)$ and $F_\infty(S)$ values is provided in Table 1 of that reference.

2.2. Use of multi-mechanism $\eta_{\rm cap,SF}$ expression to predict the performance of idealized FFs

In Paper I we used these results for the SF particle capture fraction to calculate the evolution of an aerosol population within an idealized fibrous filter comprised of a low volume fraction of equi-spaced filaments of only one size, each oriented normal to the carrier gas flow. We explicitly considered these fibers to be uniformly distributed within a filter which is thin compared to its radius of curvature, 'thick' on the scale of the mean interfiber distance, but not so thick as to cause a significant relative change in carrier gas pressure level across it. In this special case, if z is the physical distance measured into the FF medium and particle volume, $v = (\pi/6)d_{\rm p}^3$, is used in place of particle diameter, we find that the ASD-function: $n(v;z)$ should satisfy the appropriately specialized PBE:

$$\frac{\partial n}{\partial z} = -\frac{4}{\pi d_{\rm f}} \cdot \frac{\phi_{\rm f}}{1-\phi_{\rm f}} \cdot n(v,z) \cdot \eta_{\rm cap,SF} \cdot \left(1 + \frac{d_{\rm p}}{d_{\rm f}}\right) \tag{7}$$

where $U_0\times$ RHS represents the pseudo-homogeneous sink term for suspended particles with volumes between v and $v + dv$—including the explicit "interception factor" associated with the non-negligible ratio of particle-to-fiber diameter. This implies that, for such a FF challenged by an inlet aerosol ASD with any specified $n(v,0)$, a formally exact solution $n(v,z)$ to Eq. (7) may be written:

$$n(v,\zeta) = n(v,0) \cdot \exp\left[-\eta_{\rm cap,SF} \cdot \left(1 + \frac{d_{\rm p}}{d_{\rm f}}\right)\zeta\right] \tag{8}$$

in terms of the dimensionless axial variable ζ

$$\zeta \equiv \frac{4z}{\pi d_{\rm f}} \cdot \frac{\phi_{\rm f}}{1-\phi_{\rm f}} \tag{9}$$

(where for the polydispersed fiber diameter case the geometric mean fiber diameter, $d_{{\rm f},g}$, must be considered in the definition of ζ) with $\eta_{\rm cap,SF}$ evaluated using the formulation summarized in Section 2.1 above. This result[1] was used in Paper I to track the evolution of initially single-mode LN aerosol populations within a FF, as well as the expected overall performance of a FF with specified thickness, fiber diameter and solidity.

[1]While we remain focused on FFs of low solid fraction, we recommend inclusion of the factor: $(1-\phi_{\rm f})^{-1}$ in Eqs. (7–9) because, in the derivation of the steady-flow particle mass balance, while the SF-particle capture fraction determining the local volumetric particle sink strength is defined using the interstitial velocity, the net inflow of particles by convection is reduced by the fraction: $1-\phi_{\rm f}$ of the total cross section available for carrier gas flow.

2.3. Exploiting access to dimensionless "sensitivity coefficients" based on semi-analytic $\eta_{\rm cap,SF}$ results

The availability of semi-analytic results for the capture fraction of a single fiber (see Arias-Zugasti et al. (2019) and Section 2.1 above) makes it possible to explicitly express and calculate a number of valuable dimensionless coefficients which quantify the local fractional change in $\eta_{\rm cap,SF}$ associated with a small fractional change in each of the physical parameters: $d_{\rm p}$, $d_{\rm f}$, U, etc.

The first of these, i.e.:

$$\kappa_{\rm p} \equiv \frac{\partial \ln \eta_{\rm cap,SF}}{\partial \ln d_{\rm p}} \tag{10}$$

which can be explicitly expressed in terms of the basic parameters Re, Pe, R, Π, $\mathrm{Kn_p}$, was used in Paper I to investigate the accuracy of a simple 3-moment approximate method for predicting ideal FF performance when challenged by ASDs of LN shape and modest spread. In that case we exploited the fact that, locally:

$$\eta_{\rm cap}(v) \simeq \eta_{\rm cap}(\mathrm{Re}, \mathrm{Pe}_g, R_g, \mathrm{Stk}_g, \mathrm{Kn_g}) \cdot (v/v_g)^{\kappa_{\rm p}/3} \tag{11}$$

where the subscripts g in the arguments on the RHS imply evaluation of $\eta_{\rm cap}$ for particles of the local "reference" size $v_g(z)$. Invoking this local 'power-law' representation for the particle size dependence of $\eta_{\rm cap}(v)$ was shown to dramatically simplify the quadratures (over v) required to calculate the overall aerosol mass penetration of such FFs.

In what follows we will show that our access to two additional "sensitivity coefficients"—i.e. those governing the fractional change in $\eta_{\rm cap}$ to small fractional changes in fiber diameter, $d_{\rm f}$, or gas velocity, U, can also be used to enable our abovementioned predictive methods to be extended to more realistic (i.e., commercially available, 'non-ideal') FFs that exhibit measurable fiber 'dispersity' with respect to diameter, orientation, and solid fraction.

These particular extensions are of special interest here because they immediately enable direct comparisons with experimental data obtained with commercially available fibrous filter media—as illustrated below for particle size-resolved filter performance (Section 4). Encouraging comparisons of this type would open the door to future accurate predictions of FF-performance when challenged by more general polydispersed aerosol populations based on the use of an appropriately modified aerosol PBE—exhibited for the first time below. Significantly, this generalized PBE 'starting point', which incorporates rational corrections for at least these 3 microstructural features of available FF media, also admits formally exact solutions by the method we simply call 'successive quadratures', as illustrated/exploited in Section 4.

2.4. Generalization for aerosol 'morphologies' exhibiting $d_{\rm p,icpt,eff} > d_{\rm p,mob,eff}$

If the aerosol source is such that the particles being captured are not isolated dense spheres then the conventionally defined 'mobility' diameter would no longer characterize the particle's interception behavior—in effect $d_{\rm p,icpt,eff}$

could be noticeably larger than the reported particle mobility diameter. This type of disparity, which could also be the result of some particle aggregation during test aerosol preparation, is readily embraced using our present theoretical approach (Section 2) because there is no intrinsic requirement that the particle interception radius (the distance from the fiber surface where the boundary condition is actually imposed) be equal to the radius which dictates particle mobility (i.e., Brownian diffusion coefficient at the prevailing Knudsen number). In such cases (see, e.g., Section 4.1) and Eq. (10) above) we must distinguish between two different "sensitivity" coefficients—one for $\kappa_{\mathrm{p,icpt}}$ and one for $\kappa_{\mathrm{p,mob}}$, as mentioned in Appendix A. As might be expected these differences become important for sufficiently large particle "eccentricities" and have been well-recognized in situations dealing with needle-like shaped aerosol particles. Typical values of the 'expected' ratio: $d_{\mathrm{p,icpt,eff}}/d_{\mathrm{p,mob,eff}}$ for various canonical shapes, aspect ratios and Knudsen numbers are contained in Rosner & Fernandez de la Mora (2022)—a study motivated by our present conclusions (Sections 4.1 and 5) when comparing our filter performance predictions with the recent measurements of Kang et al. (2019) (who employed mobility-size selected KCl(s) particles formed by evaporating sprays of KCl solutions, as summarized in Section 4.1 below).

3. Generalization of PBE to Include Structural Features of Realistic FF Media (fiber dispersity wrt diameter, orientation and volume fraction)

3.1. Single mode LN fiber diameter pdf(d_{f}) with mono-sized particles; calculation/use of κ_{f}

SEM photographs have revealed that many commercially available FF media exhibit fiber diameter distribution functions which are nearly log-normal (LN), with geometric spread parameters, σ_g, often ≤ 2 (see, e.g., Kang et al. (2019)). Because our semi-analytic multi-mechanism SF capture fraction relation provides an explicit result (reproduced in Appendix A) for the coefficient κ_{f}, governing the sensitivity of $\eta_{\mathrm{cap,SF}}$ to small fractional changes in fiber diameter—i.e.:

$$\kappa_{\mathrm{f}} \equiv \frac{\partial \ln \eta_{\mathrm{cap,SF}}}{\partial \ln d_{\mathrm{f}}} \tag{12}$$

this implies that the local capture fraction near $d_{\mathrm{f},g}$ is proportional to $(d_{\mathrm{f}}/d_{\mathrm{f},g})^{\kappa_{\mathrm{f}}}$ and, if this local power law is invoked together with the assumed LN pdf(d_{f}), it is possible (by analytic integration) to estimate the total volumetric sink for aerosol particles of volume v per unit volume of the local FF medium—accounting for capture by fibers of *all* diameters. Recalling that our aerosol filtration PBE was previously as simple as Eq. (7) of Section 2, we now find[2] that our use of the sensitivity coefficient κ_{f} with the abovementioned LN-pdf(d_{f}) leads to the generalized DE

$$\frac{\partial n}{\partial \zeta} = -n(v,\zeta) \cdot G_{\mathrm{f}}(v) \cdot \eta_{\mathrm{cap,SF}}(v; d_{\mathrm{f},g}) \cdot \left(1 + \frac{d_{\mathrm{p}}}{d_{\mathrm{f},g}}\right) \tag{13}$$

(with the dimensionless axial variable ζ (Eq. (9)) defined in terms of the geometric mean fiber diameter, $d_{\mathrm{f},g}$) where the factor $G_{\mathrm{f}}(v)$ is found to be:

$$G_{\mathrm{f}} = \left\{ \exp\left[\frac{(\kappa_{\mathrm{f}}+1)^2 - 4}{2} \ln^2 \sigma_{\mathrm{f},g}\right] + \frac{d_{\mathrm{p}}}{d_{\mathrm{f},g}} \exp\left[\frac{\kappa_{\mathrm{f}}^2 - 4}{2} \ln^2 \sigma_{\mathrm{f},g}\right] \right\} \cdot \left(1 + \frac{d_{\mathrm{p}}}{d_{\mathrm{f},g}}\right)^{-1} \tag{14}$$

where κ_{f} (see Appendix A) is to be evaluated at the prevailing value of the particle volume $v = (\pi/6) d_{\mathrm{p}}^3$. We note that, as required, when the geometric spread, $\sigma_{\mathrm{f},g}$, of the LN population of fiber diameters reduces to unity this generalized aerosol PBE for the FF simplifies to Eq. (7) of Section 2.

3.2. Narrow Gaussian ODFs for FFs challenged with mono-sized particles; calculation/use of κ_U

In the same spirit, we briefly investigate here whether the attractive properties of our $\eta_{\mathrm{cap,SF}}$-relation can also be exploited to facilitate finding a rational FF-performance correction factor for a second *microstructural feature* of such filter media: i.e., fiber *orientation* with respect to the carrier gas flow—again for sufficiently "modest" orientation distribution function (ODF) spreads. At first sight this might seem unlikely, because the asymptotic transport analysis underlying the development of our multi-mechanism semi-analytic $\eta_{\mathrm{cap,SF}}$ relation (see, e.g., Fernandez de la Mora & Rosner (2019)) was based on aerosol capture by an isolated fiber at normal incidence—i.e.: $\theta = \pi/2$. However, that analysis does provide access to the dimensionless sensitivity coefficient:

$$\kappa_U \equiv \frac{\partial \ln \eta_{\mathrm{cap,SF}}}{\partial \ln U} \tag{15}$$

which is also explicitly given in Appendix A. If we make the reasonable assumption that, for incidence angles near $\pi/2$, what really 'counts' is the *normal* component: $U \sin\theta$, then a valid representation of $\eta_{\mathrm{cap,SF}}$ in the vicinity of normal incidence would be:

$$\eta_{\mathrm{cap,SF}}(\theta) \simeq \eta_{\mathrm{cap,SF}}(\pi/2) \cdot (\sin\theta)^{\kappa_U} \tag{16}$$

This assumption, combined with a reasonable representation of the fiber ODF, would then provide a tractable estimate of the likely capture rate consequences of fiber orientation in such filter media. With the further assumptions that: (a) pdf(θ) is near-Gaussian with spread (in radians) σ_θ about the mean value $\pi/2$, and (b) this spread is fiber diameter-insensitive—i.e. pdf(d_{f}, θ) = pdf(d_{f}) · pdf(θ), then, expanding $\sin\theta$ in the vicinity of $\pi/2$, leads to the

[2] Using the closed-form LN-result:

$$\mu_k \equiv \int_0^\infty x^k \mathrm{pdf}(x)\, dx = x_g^k \cdot \exp\left(\frac{k^2}{2} \ln^2 \sigma_g\right)$$

following rational estimate[3] of the required aerosol PBE correction factor, G_θ, to account for the ODF-effect on particle size-dependent aerosol capture

$$\eta_{\rm cap,SF}(\theta) \simeq G_\theta \cdot \eta_{\rm cap,SF}(\pi/2) \tag{17}$$

where

$$G_\theta = 1 - \frac{\sqrt{\pi}}{2}\kappa_U \left(\sigma_\theta^2 - \frac{\sigma_\theta^4}{4} + \dots\right) \tag{18}$$

Moelter & Fissan (1997) have reported structural measurements on a particular (commercially available) fiberglass HEPA filter—including an inference of the near-Gaussian pdf of gas impingement angle (relative to the mean carrier gas flow and the axis of the prevailing cylindrical fibers.) The values they report (their Fig. 13) are roughly equivalent to a Gaussian pdf(θ) centered about the expected modal value $\pi/2$, with a spread, σ_θ, of ca. 0.4 radians. This value will be provisionally used for the illustrative calculations of the abovementioned factor G_θ, as discussed in Sections 4 and 5.

3.3. Effect of meso-scale non-uniformity in the local fiber volume fraction

Even for macroscopically spatially homogeneous fibrous filters there will inevitably be local (i.e., *mesoscopic*) spatial non-uniformities in the fiber solid fraction. Such variations in fiber solid fraction will, in turn, be responsible for mesoscopic gas velocity differences, which, in turn, will cause spatial non-uniformities in the SF aerosol capture fraction. The approach introduced in Sections 3.1 and 3.2 above can also provide a rational estimate of this additional structural effect—treated (using rather different methods) by Schweers & Löffler (1994) Dhaniyala & Liu (2001) and, more recently, by Przekop & Jackiewicz-Zagórska (2020). However, to proceed along our previously recommended path, we need to invoke a plausible pdf($\phi_{\rm f}$) which will mathematically describe departures of the local solid fraction from its mean value, $\langle\phi_{\rm f}\rangle$—only the latter being readily accessible via a knowledge of both the intrinsic fiber mass density and the apparent density of a unit volume of the available FF material.

Because the maximum[4] eligible range of the fiber solid fraction, $\phi_{\rm f}$, is from 0 to 1, and the likely *skewness* of this pdf (with an expected RHS 'tail'), rather than considering a narrow, symmetrical Gaussian pdf, for this mesoscopic inhomogeneity correction calculation (and future PBE calculations) we provisionally assume a so-called *beta* pdf-fit to appropriate meso-structural data on commercially available fiberglass filters—i.e., we exploit the functional form:

$${\rm pdf}(\phi) = \frac{\phi^{\alpha-1}\cdot(1-\phi)^{\beta-1}}{B(\alpha,\beta)} \tag{19}$$

where the 2 indicated exponents, $0 < \alpha, \beta$ satisfy the normalization condition:

$$B(\alpha,\beta) \equiv \int_0^1 \phi^{\alpha-1}\cdot(1-\phi)^{\beta-1}\, d\phi = \frac{\Gamma(\alpha)\Gamma(\beta)}{\Gamma(\alpha+\beta)} \tag{20}$$

Available (apparent) density measurements combined with appropriate FF image analysis (see, e.g., Moelter & Fissan (1997)) can be used to extract the best-fit parameters α and β for this well-studied normalized pdf. In the analysis below we also exploit the fact that the lower integral moments of this distribution are known analytically[5], and the mean value, $\langle\phi_{\rm f}\rangle$, is, itself, $\ll 1$. For example, our present predictions for fiberglass filter HF-0012 are based on $\langle\phi_{\rm f}\rangle = 0.039$ and we have provisionally assumed a 'coarseness' ratio: $\sigma/\langle\phi_{\rm f}\rangle$ of ca. 0.5. These features, combined with the $d_{\rm p}$-dependent sensitivity coefficient κ_ϕ, also relatable to κ_U (see Appendix A), enable us to find/evaluate the following provisional expression for the $\phi_{\rm f}$-inhomogeneity correction factor G_ϕ, i.e.:

$$G_\phi = \frac{(1-\langle\phi_{\rm f}\rangle)\, M_{1+\kappa_\phi}}{\langle\phi_{\rm f}\rangle^{1+\kappa_\phi}} \cdot \left(1 + \frac{M_{2+\kappa_\phi}}{M_{1+\kappa_\phi}} + \dots\right) \tag{21}$$

When $|\kappa_\phi| \ll 1$ it can be shown that $G_\phi \simeq 1 + (\sigma/\langle\phi_{\rm f}\rangle)^2 \cdot \langle\phi_{\rm f}\rangle + \dots$, where σ^2 is the variance of the calculated prevailing pdf($\phi_{\rm f}$). This G_ϕ-factor estimate will appear as another multiplicative correction to $\eta_{\rm cap,SF}$ (evaluated at the mean solid fraction, $\langle\phi_{\rm f}\rangle$) in our generalized aerosol PBE for our preliminary filter performance calculations (Sections 4 and 5) based on recent particle size-specific FF capture performance experimental data (e.g., Kang et al. (2019)).

3.4. Inclusion of the consequences of pdf($d_{\rm f}$), pdf(θ), *and* pdf($\phi_{\rm f}$) *in the aerosol PBE for a realistic FF*

Accessibility of the dimensionless sensitivity coefficients characterizing the SF aerosol capture fraction (Section 2.3)

[3] Using the result:

$$\int_{-\infty}^{\infty} x^k e^{-x^2} dx = \frac{1}{2}\left(1+(-1)^k\right)\cdot\Gamma\left(\frac{1+k}{2}\right)$$

(for $k > -1$) and κ_U is generally particle-size dependent. It is interesting to note that the exponent κ_U is often negative so that, in such cases (e.g., when Brownian diffusion is the dominant capture mechanism) the correction factor for FF ODF would actually exceed unity.

[4] Actually, for a random packing of rigid circular cylinders of equal diameter, a physical upper limit to the solid fraction is set by the so-called 'jamming' or *random close packed* state, which in this case would be a number close to 0.88. This generalization would be simple to include while retaining the present beta-function formulation (by using a rescaled normalization condition based on a pdf integrand proportional to $\phi^{\alpha-1}\cdot(\phi_j-\phi)^{\beta-1}$ where, in this case, $\phi_j \simeq 0.88$.) However, both the mean FF solid fractions of practical interest and the expected pdf variance about the mean are so much smaller that the jamming limit that this refinement would not be numerically significant. Remarkably, the moment relation for the beta pdf on this modified solid fraction interval is unaltered by the choice of ϕ_j—i.e. M_k remains $B(k+\alpha,\beta)/B(\alpha,\beta)$.

[5] Indeed, inspection of Eq. (20) reveals that the kth moment of this pdf, written M_k, can immediately be written in terms of a simple ratio of the abovementioned *beta* functions; i.e.: $M_k = B(k+\alpha,\beta)/B(\alpha,\beta)$.

is seen to facilitate implementing *each* of the abovementioned FF-microstructure-dependent corrections. This encourages us to begin exploring the accuracy of a generalized aerosol population balance equation (PBE). This PBE, when combined with our multi-mechanism $\eta_{\mathrm{cap,SF}}$, should enable improved estimates of the performance of *realistic* FF media. However, for the present we are obliged to neglect conceivable 'couplings' among these 3 FF structure sensitive effects[6], leading to the simplification that the relevant correction factor (in the presence of them all) would be the prevailing product: $G_{\mathrm{f}} \cdot G_{\theta} \cdot G_{\phi}$. On this basis, and for the remainder of this study we take the applicable PBE for aerosol capture by a FF (exhibiting modest dispersity wrt fiber: d_{f}, orientation θ, and local solid fraction ϕ_{f}) to be:

$$\frac{\partial n}{\partial \zeta} = -n \cdot G_{\mathrm{f}} \cdot G_{\theta} \cdot G_{\phi} \cdot \eta_{\mathrm{cap,SF}} \cdot \left(1 + \frac{d_{\mathrm{p}}}{d_{\mathrm{f},g}}\right) \qquad (22)$$

where we recall that the dimensionless axial variable ζ is given by $\zeta = \frac{4z}{\pi d_{\mathrm{f},g}} \cdot \frac{\langle \phi_{\mathrm{f}} \rangle}{1-\langle \phi_{\mathrm{f}} \rangle}$, and where all functios in the RHS are evaluated at the nominal (mean) FF values $d_{\mathrm{f},g}$, $\langle \phi_{\mathrm{f}} \rangle$ and $\theta \simeq \pi/2$.

While our more ambitious goal is to exploit such an aerosol PBE to predict FF performance when challenged with broad (and not necessarily LN-) ASDs, for starters we can immediately exploit our proposed Eq. (22) to learn if this tractable reformulation/generalization of single-fiber-efficiency (SFE-) theory is in encouraging agreement with the recent experiments of Kang et al. (2019) for the capture of mobility-selected (KCl(s) above ca. 20 nm diam) particles challenging a commercially available fiberglass filter.

3.5. Inclusion of the consequences of $d_{\mathrm{p,icpt,eff}} > d_{\mathrm{p,mob,eff}}$ in the SF capture fraction and corresponding FF aerosol PBE

As will be discussed and quantified in Section 4.1, our present formulation also facilitates rational predictions of aerosol particle capture when the suspended particles exhibit effective interception diameters which are systematically different from the more familiar mobility diameter—an occurrence which should be expected if the suspended particles of interest are non-spherical and/or somewhat gas permeable (as for so-called 'cluster aggregates', each comprised of numerous, much smaller, granules; see, e.g., Rosner & Tandon (2018)). As indicated below and in Section 4.1, this generalization requires introduction of the additional function: $\delta(\mathrm{Kn}_{\mathrm{mob}}; \text{particle shape/morphology})$ defined by the effective diameter *ratio*: $d_{\mathrm{p,icpt,eff}}/d_{\mathrm{p,mob,eff}}$ at the prevailing Knudsen number based on particle mobility radius.

With respect to the single fiber capture fraction this means that wherever d_{p} appeared in the function $\eta_{\mathrm{cap,SF}}(\mathrm{Re}, \mathrm{Pe}, R, \Pi, S, \mathrm{Kn}_{\mathrm{p}})$ its appearance in the interception terms R and $1 + R$ should be replaced by the product $\delta d_{\mathrm{p,mob}}$. However, the evaluation of Pe remains unaltered because the slip-corrected particle diffusivity D_{p} (evaluated via $d_{\mathrm{p,mob,eff}}$) remains unaltered.

With respect to the PBE, we can imagine that the particle volume variable v_{p} is now defined by the reference value $(\pi/6)d^3_{\mathrm{p,mob}}$, but then the explicit fiber projected area term used to define $\eta_{\mathrm{cap,SF}}$ should clearly be replaced by $1 + \delta d_{\mathrm{p,mob}}/d_{\mathrm{f},g}$. Lastly, the most important filter microstructure correction term (pertaining to fiber diameter dispersity): G_{f} (Eq. (14)) must be altered to replace the ratio: $d_{\mathrm{p}}/d_{\mathrm{f},g}$ by $\delta d_{\mathrm{p,mob}}/d_{\mathrm{f},g}$ wherever it appears, and to evaluate the sensitivity coefficient $\kappa_{\mathrm{f}}(\mathrm{Re}, \mathrm{Pe}, R, \Pi, S, \mathrm{Kn}_{\mathrm{p}})$ at the appropriate values of its arguments, with the parameters R, Π and S replaced by their mobility diameter-based values, multiplied, respectively, by the $\mathrm{Kn}_{\mathrm{mob}}$-based factors δ, δ and δ^2.

4. Comparison of Present FF Aerosol Capture Efficiency Predictions with Recent Experiments

A valuable set of experimental data, based on a commercially available fibrous filter identified as HF-0012 (via Hollingsworth & Vose Co., East Walpole, MA), to test their CFD + stochastic simulation methods, has been provided by Kang et al. (2019). Because these filter efficiency measurements employed many mobility-selected KCl(s) discrete particle sizes between ca. 20 nm and 600 nm, each such data point (e.g., their Fig. 10ac) corresponds to the use of our aerosol PBE for a very special ASD, namely:

$$n(v, z) = N'''_{\mathrm{p}}(z) \cdot \delta(v - v_{\mathrm{p}}) \qquad (23)$$

where $\delta(v - v_{\mathrm{p}})$ is the Dirac delta function centered at the selected particle volume v_{p}, which, for each such experiment, is clearly z-independent. However, the local aerosol particle number density, $N'''_{\mathrm{p}}(z)$, will then decrease in accord with our generalized aerosol PBE—i.e., $N'''_{\mathrm{p}}(z)$ will satisfy the separable first order ODE Eq. (22) with the substitutions Eq. (23) and $\partial n/\partial \zeta \rightarrow dN'''_{\mathrm{p}}/d\zeta$, where $\eta_{\mathrm{cap,SF}}$ is calculated according to Section 2 and Arias-Zugasti et al. (2019) and the micro/meso-structure-sensitive correction factors: G_{f}, G_{θ} and G_{ϕ} are evaluated for the particular particle diameter $d_{\mathrm{p}} = (6v_{\mathrm{p}}/\pi)^{1/3}$ corresponding to the mobility-selected particle volume v_{p}. This implies that each experimental filter efficiency, $\eta_{\mathrm{cap,F}}$,

[6] More generally, we will need a joint (multivariate) pdf; i.e., $\mathrm{pdf}(d_{\mathrm{f}}, \theta, \phi_{\mathrm{f}})$, to account for FF-microstructure effects because we anticipate that: (*a*) smaller diam (hence less 'stiff') filaments exhibit a broader range of curvatures and, hence, orientation wrt to the carrier gas flow and (*b*) a polydispersed d_{f} distribution can itself 'cause' a pdf of solid volume fraction etc. To embrace these and other possible 'correlation' effects, we will need a practical strategy to obtain/fit such joint pdfs for each important class of widely used FF-media—a more ambitious program we leave for future work.

would be given (in terms of the filter depth $L_{\rm F}$) by:

$$\eta_{\rm cap,F} = 1 - \exp\left[-\frac{4}{\pi}\cdot\frac{\langle\phi_{\rm f}\rangle}{1-\langle\phi_{\rm f}\rangle}\cdot G_{\rm f}\cdot G_\theta\cdot G_\phi\cdot\eta_{\rm cap,SF}\cdot\left(1+\frac{d_{\rm p,icpt}}{d_{{\rm f},g}}\right)\cdot\frac{L_{\rm F}}{d_{{\rm f},g}}\right] \quad (24)$$

a form which now lends itself to direct comparison with the experimental $\eta_{\rm cap,F}$-values plotted in Kang et al. (2019) (their Fig. 10ac). In domains of particle size where the filter capture fraction approaches unity it is often more convenient to explicitly consider/plot the aerosol fraction, P, which penetrates the filter (i.e., 'escapes' capture)—a quantity simply given by $1-\eta_{\rm cap,F}$.

In this regard, because the fiber ODF for this FF has not been measured/reported, our necessarily preliminary comparisons were done under the assumption that its effective Gaussian spread, σ_θ above, is probably a number between ca. 0.3 and 0.5 radians, tentatively taken (below) to be 0.4. Similarly, our present "mesoscopic non-uniformity" corrections, $G_\phi(\alpha,\beta)$ are based on provisional assignments of α and β, consistent with the mean fiber solid fraction being reported as 0.039 (because $\langle\phi_{\rm f}\rangle = [(\beta/\alpha)-1]^{-1} = 0.039$). For the second condition we provisionally assumed the 'universality' of the Moelter & Fissan (1997)-reported normalized $d\phi_{\rm f}/dd_{\rm f}$ relation, describing the contribution that fibers of each size class make to the total volume fraction. This establishes (by integration) a corresponding functional relation between $d_{\rm f}$ and $\phi_{\rm f}$. Then, invoking the unconditional Kang et al. (2019) LN pdf of $d_{\rm f}(\phi_{\rm f})$ we can find a corresponding renormalized functional relationship for the probability distribution function pdf($\phi_{\rm f}$) and its coarseness: $\sigma/\langle\phi_{\rm f}\rangle$. The beta distribution with this $\langle\phi_{\rm f}\rangle$ and coarseness σ yields the best-fit values of the parameters α and β implicit in the provisional G_ϕ calculations below—i.e. $\alpha\simeq 3.6$ and $\beta\simeq 24.6\alpha$.

Having described our initial approximations for each of these microstructure-sensitive correction (G-) factors it is instructive to display, both the $d_{\rm p}$-dependent underlying $\eta_{\rm cap,SF}$-sensitivity coefficients $\kappa_{\rm f}$ and κ_U (Appendix A) as well as each of the G-factors, and their product, as a function of aerosol particle diameter over the entire particle size range covered in the Kang et al. (2019) experiments.

Our $\kappa_{\rm f}$ and κ_U results (using semi-log coordinates), which betray the role that aerosol capture mechanism plays, are displayed in Fig. 2. Our corresponding G results (again using semi-log coordinates) are displayed in Fig. 3. One immediately notices that for the conditions corresponding to filter HF-0012 in the experiments by Kang et al. (2019), meso-scale non-uniformity in the local fiber volume fraction has a negligible effect on the overall filter performance, at least for the moderate value of $\sigma^2 = \frac{\alpha\beta}{(\alpha+\beta+1)(\alpha+\beta)^2} \simeq 4\times10^{-4}$ (with $\alpha=3.6$, $\beta=24.6\alpha$) considered here. On the other hand the effects of non-uniformity in the local fiber orientation has a small but non-negligible effect, while fiber diameter non-uniformity is clearly the dominant correction.

Assembling these results, and invoking our "single particle size" aerosol population balance Eq. (24) above, we are in a position to compare our semi-analytic predictions of filter performance, i.e. the $d_{\rm p}$-dependent *filter* capture fraction $\eta_{\rm cap,F}$, with the experimental values reported in Kang et al. (2019) over the nominal KCl(s) particle diameter range: 20-500 nm.

These comparisons, which at present are limited to filter HF-0012 at carrier gas velocities of 15 and 10 cm/s (velocities at which the effects of particle *inertia* are found to be negligible[7], even for the largest particles considered here) were carried out first, with instructive preliminary results summarized in Figs. 4a, 4b. As discussed below, these comparisons led us to consider relaxing the (previously implicit) simplifying assumption that the effective particle diameter for *interception* can be equated the stated *mobility* diameter. Clearly, this equality is only valid if the suspended particles (of any size) being captured are perfect spheres—hardly the most commonly encountered situation in aerosol applications.

4.1. Preliminary test of semi-analytic, multi-mechanism aerosol capture theory, including both FF microstructure non-idealities and possible aerosol particle 'morphological' effects

As noted above, in our first round of calculations we examined the (frequently implicit) assumption that the effective *interception* diameter of the aerosol particle, written, $d_{\rm p,icpt,eff}$, is equal to its *mobility* diameter (written $d_{\rm p,mob,eff}$). This set of capture fraction predictions, including the FF microstructure corrections of Section 3, was found to be quite successful for the Brownian-diffusion controlled regime (ca. $20 < d_{\rm p,mob,eff} < 100$ nm) but led to significant underestimates of filter capture fractions when interception became important (ca. $100 < d_{\rm p,mob,eff} < 500$ nm diam).

This observation led us immediately to the realization that, especially for non-spherical aerosol (vs. hydrosol) capture, there is little reason to expect $d_{\rm p,icpt,eff} = d_{\rm p,mob,eff}$. Qualitatively, gas slip is more likely to noticeably alter the mobility diameter than the effective interception diameter. Because the experimental data we are treating is reported in terms of particle mobility diameter, we should also consider the distinct possibility that $d_{\rm p,icpt,eff}$ is systematically different from the mobility diameter—fortunately, a generalization readily accommodated (but previously not exploited!) in our present semi-analytic "single-fiber" capture fraction formulation (Section 2 and Arias-Zugasti et al. (2019); Fernandez de la Mora & Rosner (2019).)

In the absence of previously published particle characterization information we therefore examined the simplest possibility: viz. the ratio: $\delta \equiv d_{\rm p,icpt,eff}/d_{\rm p,mob,eff}$ is

[7] However, especially as indicated by the $d_{\rm p}$-dependence of $G_{\rm f}$ (cf. Eq. (14)) the particle capture mechanism of *interception* becomes non-negligible above ca. $d_{\rm p} = 100$ nm.

greater than unity and only weakly $\mathrm{Kn}_{\mathrm{p,mob}}$-dependent[8]. Accordingly, we determined the δ-value that would 'best-fit' the presently available filter capture fraction data. Pooling the data for filter HF-0012 at both face velocities we found that the choice $\delta \simeq 2.185$ performed quite well (as shown in Fig. 4).

Pending further morphological information on the KCl(s) particles generated/mobility-selected in the experimental data examined here we note that the presently 'inferred' estimate: $d_{\mathrm{p,icpt,eff}}/d_{\mathrm{p,mob,eff}}(500\mathrm{nm}) \simeq 2$ could quite plausibly be due to a combination of non-sphericity, and/or gas permeability of cluster aggregates (see: e.g., Rosner & Tandon (2018)). However, based on the tractable particular cases we have examined theoretically—which include impermeable regular polyhedra and prolate spheroids (Rosner et al. (2022)), δ-values as large as 2 are more likely to be associated with particle "eccentricity" than "gas permeability" (as in the case of porous fractal-like, quasi-spherical cluster aggregates).

4.2. Generalizations required to predict the performance of fibrous filters in the 'nano-particle' diameter range below 20 nm diam

While a valuable data set (for the capture of size-selected Ag(s) nanoparticles between ca. 20 nm and 3 nm diam for filter HF-0012 at $U_0 = 15$ cm/s) has been provided by Kim et al. (2007), in our judgement its inclusion here would be premature for the following reasons. In addition to the presence of a significant filter performance correction associated with fiber dispersity (wrt diam, orientation and solid fraction; Section 3), two fundamental assumptions which facilitated our present semi-analytical theoretical approach (Section 2) to the single fiber capture fraction are expected to fail in the abovementioned nanoparticle regime. One is the explicit assumption: $\mathrm{Pe}_{\mathrm{f}}^{1/3} \gg 1$ (used to enable thin diffusion boundary layer theory to be applied to the PDE governing the local particle concentration field). The second assumption that will require further attention is that of *diffusion-controlled* particle capture, or "perfect capture"—i.e. the imposed boundary condition that the local particle concentration is brought to zero one particle radius away from the fiber surface. To avoid the premature 'convolution' of three systematic effects, each requiring further study, in what follows we deliberately focus on the size-selected KCl(s) data of Kang et al. (2019) above ca. 20 nm diam—where $\mathrm{Pe}_{\mathrm{f}}^{1/3}$ exceeds at least 3 and significant departures from "diffusion-controlled" capture are less likely. A self-consistent re-assessment of the np-data of Kim et al. (2007) based on a suitably generalized single fiber capture fraction is the focus of work currently in progress (Rosner et al. (2022)).

[8] In this connection it is interesting to note that for "tumbling solid cubes" (i.e., hexahedra), for which we would expect that $d_{\mathrm{p,icpt,eff}}$ is close to the diameter of the circumscribed sphere, we estimate that over the entire Knudsen transition from continuum (c-) to the free-molecule (fm-) limit, the expected icpt/mob diameter ratio δ would be adequately represented by the nominal choice: 1.3 to within better than ± 2 pct over the entire range of $\mathrm{Kn}_{\mathrm{p,mob}}$-values. Expected $d_{\mathrm{p,icpt,eff}}/d_{\mathrm{p,mob,eff}}$- ratios for several canonical particle shapes and aspect ratios are explicitly considered in Rosner & Fernandez de la Mora (2022).

5. Consequences of Fiber Dispersity wrt Diameter Orientation and Volume Fraction, with Implications for the Treatment of Fibrous Filters Challenged by Polydispersed (Size, Shape) Aerosol Populations

Our principal focus in this study has been to determine whether our presently developed / estimated FF-microstructure-sensitive 'corrections' (Sections 3.1, 3.2, 3.3) when introduced into a generalized FF- population balance equation Section 3.4 would enable our previously 'idealized' but multi-mechanism Fibrous Filter analysis (Rosner & Arias-Zugasti (2021)) to provide performance predictions which are in acceptable agreement with recently reported experimental results (on commercially available fiberglass filters challenged by mobility-selected KCl(s) aerosol particles larger than ca. 20 nm diam.).

The situation we encounter when it is first assumed that all mobility-selected aerosol particles being captured are spherical (curves simply marked $\delta = 1$, indicating that $d_{\mathrm{p,icpt}} = d_{\mathrm{p,mob}}$) is clearly displayed in Figs. 4a, 4b—which also include the experimental data points for fiberglass filter HF-0012 capture fractions at pre- selected mobility diameters (Kang et al. (2019)). If $G_{\mathrm{f}} \cdot G_\theta \cdot G_\phi = 1$ and $\delta = 1$, our '*ideal*' FF would perform as indicated by the bold *dashed* curve. However, using our present estimates of the individual $d_{\mathrm{p,mob}}$-sensitive FF microstructure corrections, we generate the corresponding predicted Filter capture fractions shown as the dark black curve, marked '*real*' FF Theory; $G_{\mathrm{f}} \cdot G_\theta \cdot G_\phi < 1$, $\delta = 1$. For both face velocities we see that our present estimates of filter capture fraction performance are quite encouraging in the domain from ca. 20-100 nm dominated by the particle capture mechanism of *Brownian diffusion*. However, for particle mobility diameters between ca. 100 nm and 500 nm, where the capture mechanism of '*interception*' becomes quite important, we are significantly *under*predicting the overall filter capture fractions. Perhaps the simplest way to account for this behavior is to investigate the possibility that the particles being studied exhibit effective interception diameters that are larger than their reported mobility diameters by a calculable factor. Indeed, we find that both data sets apparently exhibit particle capture behavior consistent with a $d_{\mathrm{p,icpt}}/d_{\mathrm{p,mob}}$-ratio of ca. 2.2—as indicated by the grey-shaded continuous curves. Remarkably, this combination of plausible physical effects appears to provide current 'predictions' which agree with these measured filter capture fractions over the *entire* mobility-diameter range (20-500 nm) studied.

These preliminary findings have already set off a number of complementary studies, which include the nature of the function: $\delta(\mathrm{Kn}_{\mathrm{mob}}; \text{particle shape/morphology})$ for

various test aerosol sources, as well as further methods to improve the accuracy of the abovementioned $G_{\rm f} \cdot G_{\theta} \cdot G_{\phi}$-product for use in the generalized PBE governing "realistic" fibrous filter performance. Our present 'path' (via a semi-analytic, multi-mechanism SF-theory, as summarized in Section 2) is encouraging because it appears to enable accessible calculations of realistic FF performance. However, further theoretical ideas (hopefully stimulated by this account of our most recent work), together with further comparisons with experimental data of the type provided in Kang et al. (2019), will be needed to further advance the approach initiated here.

While knowledge gaps and possible further improvements have been identified at each stage, we provisionally conclude from Figs. 4a, 4b (Section 4.1) that our present approach remains quite promising—without invoking aerosol transport mechanisms other than Brownian diffusion, carrier gas convection, interception (when the ratio: $d_{\rm p,icpt,eff}/d_{\rm f}$ becomes appreciable), and subcritical particle inertial effects. As was already noted in the paper containing the experimental data used in our present comparisons (i.e. Kang et al. (2019), loc cit), we also find that of the identifiable FF-structural "realities", the effect of fiber diameter dispersity is more significant than corresponding nonuniformities in fiber orientation and local solid fraction. The ability of our present formulation to not only efficiently account for the interactions among these aerosol capture mechanisms, while incorporating the presently recognized disparity between the effective interception– and mobility- diameters for aerosol particles of 'modest' eccentricity, are especially noteworthy. Further comparisons of this type are recommended, but it will also be instructive to examine the consequences of our present PBE approach when dealing with the filtration of aerosol populations which are dispersed with respect both particle size and morphology.

6. Conclusions, Recommendations and Future Work

Recently obtained semi-analytic solutions to field equations governing the multi-mechanism aerosol capture behavior of a single cylindrical fiber in low Re-crossflow (Fernandez de la Mora & Rosner (2019), and Arias-Zugasti et al. (2019)) have been summarized in Section 2. In our paper I (Rosner & Arias-Zugasti (2021)) we showed that this formulation for $\eta_{\rm cap,SF}$, when combined with an idealized structural model of fibrous filters (i.e., viewing each such filter as a pseudo-homogeneous, spatially uniform 'deep forest' of single-diameter fibers in crossflow) can be used to predict filter capture fraction behavior even for arbitrary inlet particle size distributions, $n(v,0)$. In the present work we have explored (Section 3) a tractable route to enable our methods to be generalized to account for three notable structural features of 'real' fibrous filters, viz., dispersity in fiber: diameter, orientation, and volume fraction. We exploit here our previously discussed access to dimensionless *sensitivity coefficients* characterizing the single-fiber aerosol capture fraction—in particular, the coefficients $\kappa_{\rm f}$ and κ_U, quantifying the local fractional response of $\eta_{\rm cap,SF}$ to modest fractional changes in fiber diameter, $d_{\rm f}$, and/or carrier gas velocity, U. Combined with potentially measurable, and appropriate distribution functions (quantifying the dispersity of fiber: diameter, orientation, and solid fraction), we propose a generalized aerosol population balance equation (PBE) which admits formally exact solutions for the evolution of the aerosol particle number density distribution function, $n(v,z)$, within such filters by our previously described (Paper I) method of 'successive quadratures', even for arbitrary initial aerosol size distributions: $n(v,0)$. Here we have initiated testing our semi-analytic predictive methods, by comparison with the recent experimental data of Kang et al. (2019) for a particular class of commercially available FFs challenged by a succession of mono-sized (KCl(s)) particles covering the range of mobility diameters from ca. 20 nm to 600 nm.

As explained in Sections 4, 5, the comparison between the present theoretical model and the experimental results by Kang et al. (2019) led us to the realization that these data suggest the necessity of relaxing the assumption that the effective particle interception diameter is equal to the particle mobility diameter, an assumption which is only valid for spherical particles. In this regard, the present theoretical model allows for a simple overall description of particle non-sphericity effects by means of a single dimensionless parameter, δ, defined as the ratio between the particle effective interception diameter and mobility diameter. Thus, the experimental particle capture data by Kang et al. (2019) have been used to determine a best fit for this parameter, leading to $\delta \simeq 2.2$. Based on this least squares fit for δ the comparison with the experimental results by Kang et al. (2019) loc. cit. with the present theoretical model (including the correction factors related to fiber dispersity wrt fiber diameter and orientation) shows a remarkable agreement regardless of particle size. On the other hand, the theoretical predictions neglecting the fiber dispersity wrt diam and orientation corrections are clearly less accuate, showing that small changes in fiber diameter and orientation can produce significant changes in overall filter efficiency.

Further generalization of our predictive methods, along with instructive comparisons with additional data Kim et al. (2007), are currently in progress (especially to apply to the FF penetration results reported for Ag-nanoparticles in the size range 20 to 3 nm.)[9] These valuable data will re-examined and re-assessed using methods rather different from those employed by Wang et al. (2007).

[9] In this particle size range systematic generalizations of our present theory-based formulation are needed to account for the expected breakdown of two underlying assumptions exploited in Section 2, viz. $\mathrm{Pe}^{1/3} \gg 1$ and the diffusion-limited boundary condition: $N'''_{\rm p,w} = 0$.

It should be kept in mind that while our present methods incorporate the intrinsic couplings that occur among the particle capture mechanisms of convective-diffusion, interception and particle inertia, in dealing with commercially available fibrous filters we have chosen to illustrate our semi-analytical FF-performance prediction methods by explicitly invoking the distinctly simplifying assumption of near-independence of each of the 3 most relevant FF- structure state variables and their associated plausible univariate *microstructure* pdfs. A more general multivariate joint pdf path (to include the likely couplings mentioned in Section 3) may indeed become important, and feasible, in the foreseeable future.

In any case, the generality, versatility and comparative simplicity of our present predictive methods, and the encouraging preliminary comparison with the experimental results of Kang et al. (2019) discussed in Sections 4 and 5, suggest that, with further development/testing, they should be able to provide the basis for useful fibrous filter performance predictions in both industrial- and public health- settings over a wide variety of operating conditions—including even gas velocities high enough to exploit the (often overlooked) capture mechanism of subcritical particle inertia. This mechanism, as distinct from *direct impaction*, occurs for $\mathrm{Stk_p} \cdot C(\mathrm{Re}) < 2.21485$, and has been shown (Rosner & Arias-Zugasti (2021) and Arias-Zugasti et al. (2019)) to be capable of significantly reducing the penetration of particles which would have escaped capture by only *pure* Brownian diffusion and interception.

In contrast to many currently proposed CFD-based particle tracking simulations (see, e.g., Hosseini & Vahedi Tafreshi (2010), Gervais et al. (2015) and, more recently, Kang et al. (2019)) which, in effect, comprise *numerical experiments*, our present semi-analytical methods also provide a rational- and economical- 'correlation scheme' which has current/future predictive value. Our present methods/results lead directly to Eq. (24) for the expected fibrous filter capture fraction, $\eta_{\mathrm{cap,F}}$, which also includes our suggested approach to correct for FF-structural features via the explicit factors G_{f}, G_θ and G_ϕ (Section 3), depending on effective particle mobility and interception diameters. Perhaps most important, the present work provides explicit functional expressions (in terms of the physically relevant dimensionless parameters in the system) for the filter capture fraction, $\eta_{\mathrm{cap,F}}$, as well as the filter dispersity related correction factors, bringing us closer to our collective ultimate goal: viz., to enable designers and users of fibrous filters to make timely operational- or acquisition-decisions based on tractable in-house calculations at everyone's disposal.

Nomenclature

Symbol	**definition**
a	radius (of particle or fiber)
A	cross-sectional area of fibrous filter (assumed constant)
d	diameter ($d = 2a$)
D_{p}	Brownian diffusivity (slip-modified Stokes-Einstein), $D_{\mathrm{p}} = C_s k_B T / (6\pi\mu_g a_{\mathrm{p,mob}})$
C_s	Cunningham-Millikan slip factor (fct(Kn)) for isolated solid sphere drag
C	Oseen-Stokes function of Re, $C \equiv \left[1 + \ln \mathrm{Re}^{-1/2}\right]^{-1}$
E	inertial enrichment fct. of S for forward stagnation line
F	dimensionless mass transfer coefficient, function of only Π and S; see Arias-Zugasti et al. (2019)
f_0	function defined by Eq. (2)
f_1	function defined by Eq. (3)
G	correction factors (d_{p} dependent) for FF microstructure (Section 3)
Kn	Knudsen number ($\ell_g / a_{\mathrm{p,mob}}$)
K	$1.612\mathrm{Kn_p}$
ℓ_g	molecular mean-free-path (in carrier gas)
L_{F}	depth of fibrous filter
m	function of only Π defined by Eq. (6)
M_k	kth moment of $n(v,z)$ with respect to v
n	particle number density distribution function ($n = n(v,z)$)
N_{p}'''	local total particle number density
p	pressure level
P	aerosol fractional penetration, $P = 1 - \eta_{\mathrm{cap,F}}$
Pe	Peclet number, $\mathrm{Pe} \equiv U d_{\mathrm{f}} / D_{\mathrm{p}}$
R	interception parameter, $R \equiv a_{\mathrm{p,icpt}} / a_{\mathrm{f}}$
Re	Reynolds number, $\mathrm{Re} \equiv U d_{\mathrm{f}} / \nu_g$
S	Effective Stokes number, $S \equiv C(\mathrm{Re}) \cdot \mathrm{Stk} = (\rho_{\mathrm{p}}/\rho_g) \cdot (C_s(\mathrm{Kn_p})/9) \cdot R^2 \cdot C(\mathrm{Re}) \cdot \mathrm{Re}$
Sc	Schmidt number for particle Brownian diffusion in carrier gas, $\mathrm{Sc} \equiv \nu_g / D_{\mathrm{p}}$
Stk	Stokes number, $\mathrm{Stk} \equiv \tau / (a_{\mathrm{f}}/U)$
T	absolute temperature (Kelvins)
U	local mainstream velocity of carrier gas
v	particle volume
z	distance measured into the FF ($z = 0$ at upstream face)
Z	function of only Π, defined by Eq. (4)

Greek letters

α, β	parameters in the univariate beta

	distribution function (Eq. (19))
δ	interception over mobility particle diameter ratio, $\delta = d_{\mathrm{p,icpt,eff}}/d_{\mathrm{p,mob,eff}}$
$\delta(v - v_{\mathrm{p}})$	Dirac delta function centered at the selected particle volume v_{p}
Γ	gamma function (1 argument), incomplete Γ function (2 args.)
ϕ	local solid volume fraction
$\eta_{\mathrm{cap,SF}}$	capture fraction (based on SF frontal area of $d_{\mathrm{f}} + d_{\mathrm{p,icpt}}$ per unit length)
μ_k	kth moment of normalized pdf
μ_g	Newtonian viscosity of carrier gas
ν	momentum diffusivity (kinematic viscosity), $\nu \equiv \mu_g/\rho_g$
κ_{p}	sensitivity coefficient wrt particle size: $\kappa_{\mathrm{p,mob}} = \partial \ln \eta_{\mathrm{cap,SF}}/\partial \ln d_{\mathrm{p,mob}}$ $\kappa_{\mathrm{p,icpt}} = \partial \ln \eta_{\mathrm{cap,SF}}/\partial \ln d_{\mathrm{p,icpt}}$
κ_{f}	sensitivity coefficient wrt fiber diameter $\partial \ln \eta_{\mathrm{cap,SF}}/\partial \ln d_{\mathrm{f}}$
κ_{ϕ}	sensitivity coefficient wrt fiber volume fraction $\partial \ln \eta_{\mathrm{cap,SF}}/\partial \ln \phi_{\mathrm{f}}$
κ_U	sensitivity coefficient wrt carrier gas $\partial \ln \eta_{\mathrm{cap,SF}}/\partial \ln U$
Π	Interception-diffusion parameter here $\Pi \equiv R \cdot (\mathrm{Pe}\, C(\mathrm{Re}))^{1/3}$
ρ	mass density
σ	spread parameter (standard deviation) of univariate pdf
σ_g	spread parameter of LN $\mathrm{pdf}(v) = n(v)/N_{\mathrm{p}}'''$
τ	characteristic particle "stopping time" in prevailing viscous medium
θ	local angle between carrier gas velocity and fiber axis
ζ	dimensionless distance measured into the FF (Eq. (9))

Subscripts and superscripts

crit	critical (singular) value
cap	capture (by filament targets)
eff	effective value
f	pertaining to filament
F	pertaining to overall fibrous filter
g	pertaining to the carrier gas
g	pertaining to the geometric mean (LN pdf)
icpt	interception
mob	mobility
p	pertaining to the (solid-like) particles
s	pertaining to "slip" at gas/solid interface
sp	evaluated at the forward stagnation point
U	pertaining to the carrier gas velocity
0	in the gas immediately upstream of the filter face
0	evaluated at $\Pi = 0$ in F_0
ϕ	pertaining to the solid volume fraction
∞	evaluated at $\Pi = \infty$ in F_∞

Acronyms, Abbreviations

ASD	aerosol size distribution
CFD	computational fluid dynamics
FF	fibrous filter (here non-woven)
LBL	laminar boundary layer
LN	log-normal ASD
MPPS	maximum penetration particle size
MTBL	mass transfer boundary layer
NDDF	number density distribution function
ODE	ordinary differential equation
ODF	orientation distribution function (Section 3.2)
PDE	partial differential equation
PBE	population balance equation
pdf	probability density function (normalized, univariate)
RHS	right-hand side (of equation)
SEM	scanning electron microscope
SF	single fiber
STP	standard (reference) temperature and pressure (here 298K, 1 atm)
wrt	with respect to

Operators

$\Delta(\,)$	change in $(\,)$
$\langle\,\rangle$	spatial average value (first moment of its pdf)

Acknowledgements

It is a pleasure to acknowledge many fruitful discussions with Prof. Juan Fernández de la Mora (Yale University). Supported, in part, by Ministerio de Ciencia e Innovación (PID2019-108592RB-C44) and UNED funding for open access publishing.

References

Arias-Zugasti, M., Rosner, D. E., & Fernandez de la Mora, J. (2019). Low Reynolds number capture of small particles on a cylinder by diffusion, interception, and inertia at subcritical stokes numbers:

Numerical calculations, correlations, and small diffusivity asymptote. *Aerosol Science and Technology*, *53*, 1367–1380.

Dhaniyala, S., & Liu, B. (2001). Theoretical modeling of filtration by nonuniform fibrous filters. *Aerosol Science and Technology*, *34*, 170–178.

Fernandez de la Mora, J., & Rosner, D. E. (2019). Low Reynolds number capture of small particles on cylinders by diffusion, interception, and inertia at subcritical stokes numbers. *Aerosol Science and Technology*, *53*, 647–662.

Gervais, P.-C., Bourrous, S., Dany, F., Bouilloux, L., & Ricciardi, L. (2015). Simulations of filter media performances from microtomography-based computational domain. experimental and analytical comparison. *Computers & Fluids*, *116*, 118–128.

Hosseini, S., & Vahedi Tafreshi, H. (2010). 3-d simulation of particle filtration in electrospun nanofibrous filters. *Powder Technology*, *201*, 153–160.

Kang, S., Lee, H., Chan Kim, S., Chen, D.-R., & Pui, D. (2019). Modeling of fibrous filter media for ultrafine particle filtration. *Separation and Purification Technology*, *209*, 461–469.

Kim, S., Harrington, M., & Pui, D. (2007). Experimental study of nanoparticles penetration through commercial filter media. *Journal of Nanoparticle Research*, *9*, 117–125.

Moelter, W., & Fissan, H. (1997). Structure of a high efficiency glass fiber filter medium. *Aerosol Science and Technology*, *27*, 447–461.

Przekop, R., & Jackiewicz-Zagórska, A. (2020). Effect of mesoscale inhomogeneity and fibers size distribution on the initial stage of deep-bed filtration process. *Journal of Aerosol Science*, *142*, 105522.

Rosner, D. E., & Arias-Zugasti, M. (2021). Predicting the aerosol capture characteristics of fibrous filters. I. exact- and tractable (3-moment) approximate-methods to incorporate aerosol polydispersity effects with a multi-mechanism, semi-analytic single-fiber particle capture fraction. *Separation and Purification Technology*, *257*, 1–14.

Rosner, D. E., Arias-Zugasti, M., & Fernandez de la Mora, J. (2022). Re-examination of the theory of nanoparticle capture by fibrous filters; inclusion of the effects of 'thermal rebound' and $\mathrm{Pe}^{1/3} = \mathcal{O}(1)$. *Separation and Purification Technology*, . In preparation.

Rosner, D. E., & Fernandez de la Mora, J. (2022). By what factor can the effective aerosol 'interception'-diameter exceed the measured mobility-diameter? role of external particle shape and/or internal porosity. *Aerosol Science and Technology*, . In preparation.

Rosner, D. E., & Tandon, P. (2018). Aggregation- and rarefaction-effects on particle mass deposition rates by convective-diffusion, thermophoresis or inertial impaction: Consequences of multi-spherule 'momentum shielding'. *Aerosol Science and Technology*, *52*, 330–346.

Schweers, E., & Löffler, F. (1994). Realistic modelling of the behaviour of fibrous filters through consideration of filter structure. *Powder Technology*, *80*, 191–206.

Wang, J., Chen, D., & Pui, D. (2007). Modeling of filtration efficiency of nanoparticles in standard filter media. *Journal of Nanoparticle Research*, *9*, 109–115.

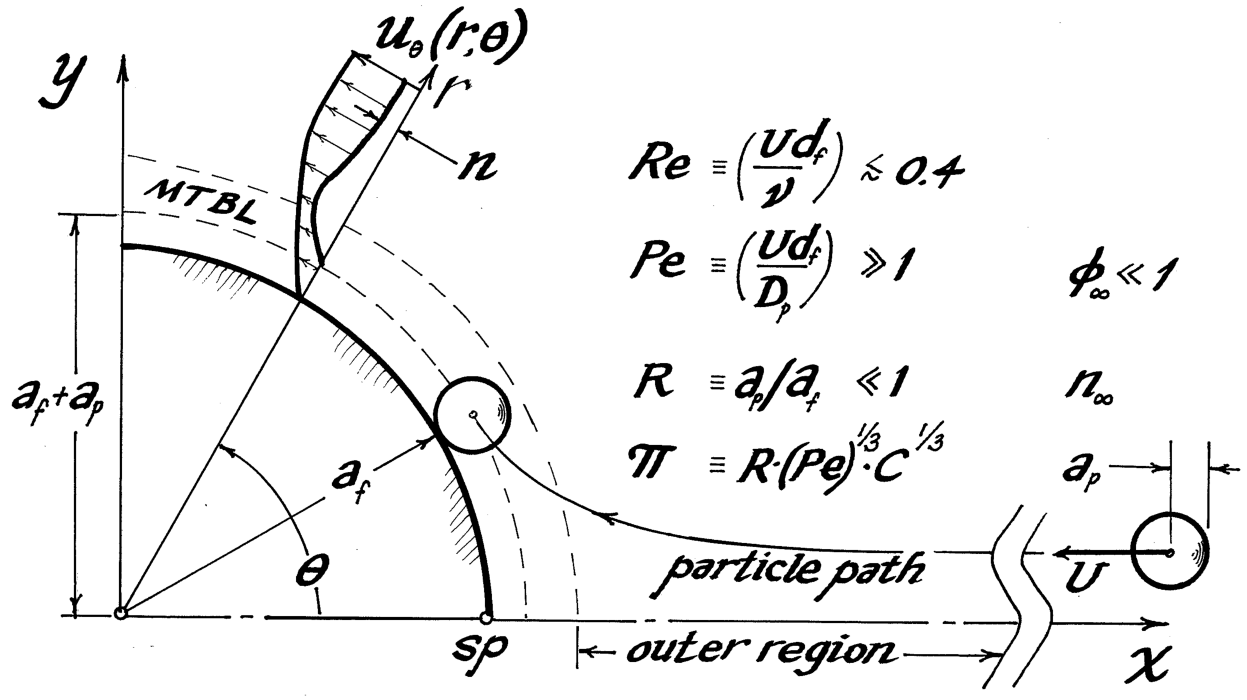

Figure 1: Schematic of the particle transport configuration and principal notation underlying our "single fiber" capture fraction analysis (after Arias-Zugasti et al. (2019), Rosner & Arias-Zugasti (2021)). While the aerosol particle depicted is a dense sphere, in practice (see, e.g. Sections 2.4 and 4.1) it may be non-spherical and exhibit an effective diameter for interception systematically larger than its reported 'mobility' diameter. This important generalization is readily incorporated in our present single fiber aerosol capture analysis (Section 2 and Appendix A)—with the relevant interception radius simply being the effective location at which the non-spherical particle's concentration is brought to zero.

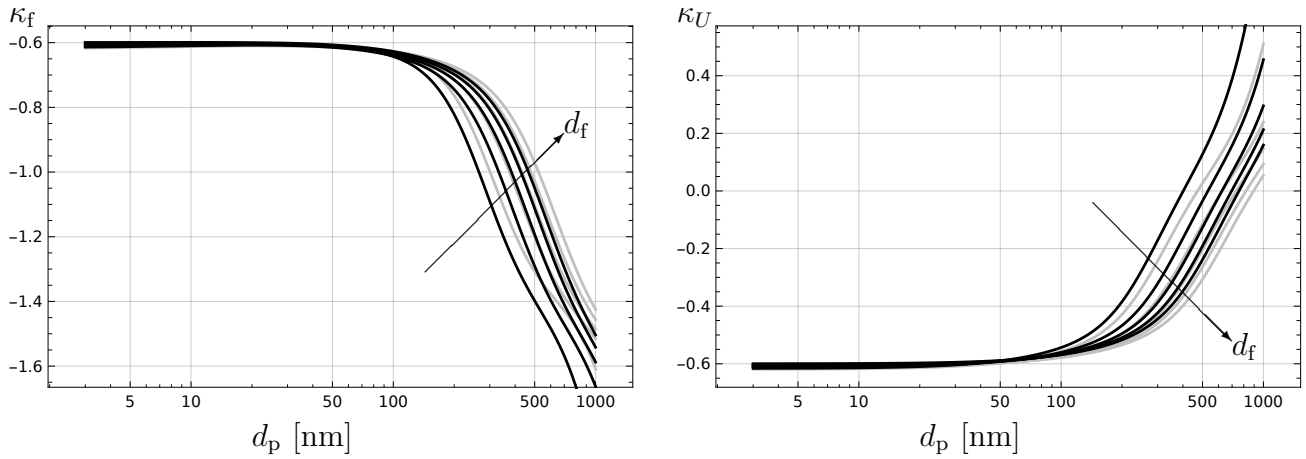

Figure 2: Numerical results for sensitivity coefficient κ_f (left) and κ_U (right) vs. particle diameter d_p [nm] for fiber diameter $d_\mathrm{f} = 1, 2, 3, 4, 5$ μm, computed according to the conditions considered by Kang et al. *Sep. Purif. Technol.* 209 (2019) 461-469 (filter HF-0012: $\phi_\mathrm{f} = 0.039$, $U_0 = 0.15$ m/s (black curves) and $U_0 = 0.10$ m/s (gray curves).)

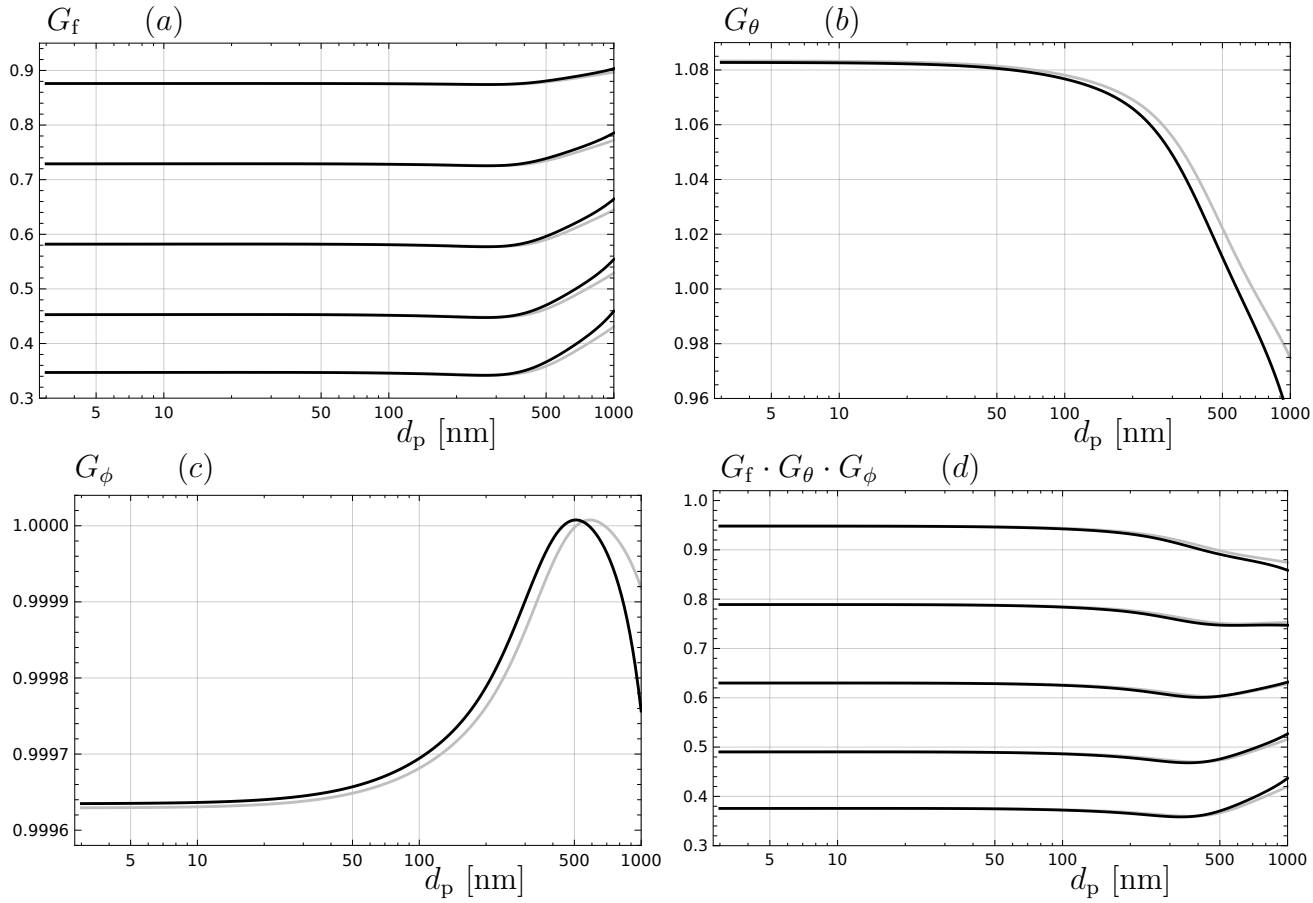

Figure 3: Numerical results for G_f (a), G_θ (b), G_ϕ (c) and $G_\mathrm{f} \cdot G_\theta \cdot G_\phi$ (d) vs. particle diameter d_p [nm] for fiber diameter $d_{\mathrm{f},g} = 2.5$ μm, $\sigma_{\mathrm{f},g} = 1.3, 1.5, 1.7, 1.9, 2.1$, $\sigma_\theta = 0.4$, $\alpha = 3.6$, $\beta = 24.6\alpha$ and $\langle \phi_\mathrm{f} \rangle = 0.039$. Black curves correspond to $U_0 = 0.15$ m/s and gray curves to $U_0 = 0.10$ m/s.

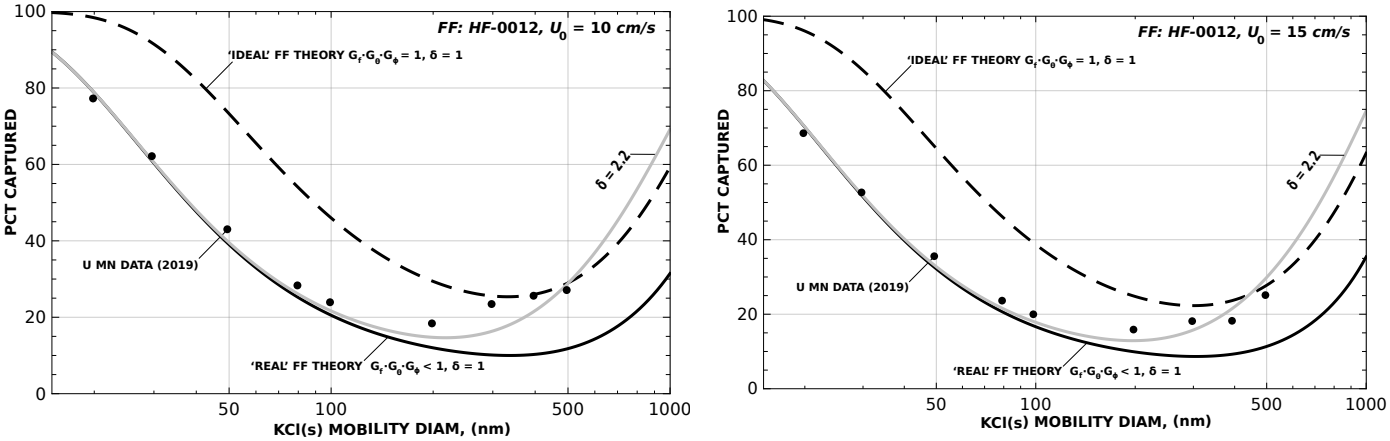

Figure 4: Predictions of the present model for filter efficiency (%) under the conditions reported by Kang et al. *Sep. Purif. Technol.* 209 (2019) 461-469 for filter HF-0012 (dots, left: $U_0 = 10$ cm/s, see Kang et al. Fig. 10a; right: $U_0 = 15$ cm/s, see Kang et al. Fig. 10c). Solid (resp. dashed) curves: results based on present model *including* (resp. *neglecting*) filter fiber dispersity wrt diam. (with $\sigma_{f,g} = 2.1$) and orientation. Solid gray lines include both, FF dispersity wrt diam. *and* non-spherical particle effects, based on particle interception/mobility diam. ratio (δ) determined by a least squares fit wrt. the experimental results by Kang et al., yielding $\delta = 2.185$.

Appendix A. Explicit Results for the Dimensionless Sensitivity Coefficients κ_{f} and κ_U Based on Semi-Analytical Multi-Mechanism $\eta_{\mathrm{cap,SF}}$ expression

The quasi-separable structure of our semi-analytic result for the multi-mechanism single fiber capture fraction (Eq. (1) of Section 2) along with the definitions each of the dimensionless parameters (Re, Pe, R, S, $\mathrm{Kn_p}$) entering these functions, enables explicit calculation of several important dimensionless *sensitivity coefficients* (we recall that our dimensionless sensitivity coefficients—e.g., Eq. (12), Eq. (15), remain unchanged in value if the relevant diameters or velocity were normalized by constant reference quantities.) Of special interest here are κ_{f} and κ_U, which, as shown in Sections 3.1-3.3, appear as local exponents in describing the effects (on SF capture fraction) of fiber dispersity with respect to diameter-, (through-plane) orientation- and solid fraction. Each of these sensitivity coefficients is particle-size-dependent via the particle size dependence of each of the abovementioned governing dimensionless parameters: Re, Pe, R, S and $\mathrm{Kn_p}$.

As in the case of κ_{p}, which was provided and exploited in Paper I Rosner & Arias-Zugasti (2021)[10] for the special case of dense spherical aerosol particles[11], we note that, by taking the logarithm of Eq. (1), it is also possible to express κ_{f} as the sum of contributions from each of the factors appearing in Eq. (1), i.e.:

$$\kappa_{\mathrm{f}} = \kappa_{\mathrm{f},0} + \kappa_{\mathrm{f},1} + \kappa_{\mathrm{f},E} + \kappa_{\mathrm{f},F} \tag{A.1}$$

Each of these contributions can now be explicitly expressed (using the 'chain rule' for differentiation) and is displayed below. Once again, we have exploited two accurate approximations, viz.: Eq. (5) for $F(\Pi, S)$ including its suggested expression for the exponent $m(\Pi)$, and, for brevity, we introduce the notation $E' \equiv dE/dS$, $F_0' \equiv dF_0/dS$, etc. below. In this way we find, and have employed, the additive contributions:

$$\kappa_{\mathrm{f},0} = \frac{1}{3}\left(\frac{C(\mathrm{Re})}{2} - 2\right) + \frac{R}{1+R} \tag{A.2}$$

$$\kappa_{\mathrm{f},1} = \frac{1}{3}\left(\frac{C(\mathrm{Re})}{2} - 2\right)\left(Z - \frac{\Pi^3}{2}\right) \tag{A.3}$$

$$\kappa_{\mathrm{f},E} = S\frac{E'}{E}\left(\frac{C(\mathrm{Re})}{2} - 1\right) \tag{A.4}$$

$$\kappa_{\mathrm{f},F} = -\frac{5}{9}m\,(1-m)\ln\left(\frac{F_0}{F_\infty}\right)\left(\frac{C(\mathrm{Re})}{2} - 2\right) + S\left[m\frac{F_0'}{F_0} + (1-m)\,\frac{F_\infty'}{F_\infty}\right]\left(\frac{C(\mathrm{Re})}{2} - 1\right) \tag{A.5}$$

Similarly, as explained/outlined in Sections 3.2, 3.3, the sensitivity coefficient κ_U can be used to predict the correction for fiber orientation distribution, as well as the correction for *meso-scale* solid fraction inhomogeneity. While the fiber solid fraction parameter ϕ_{f} does not explicitly appear in our 'single-fiber' theory (Fernandez de la Mora & Rosner (2019)), because $U = U_0/\,(1-\phi_{\mathrm{f}})$ and U_0 is constant, it is straightforward to show that

$$\kappa_\phi = \frac{\phi_{\mathrm{f}}}{1-\phi_{\mathrm{f}}}\kappa_U \tag{A.6}$$

Accordingly, κ_ϕ inherits the sign of κ_U but, in a small ϕ_{f} FF theory, $|\kappa_\phi| \ll |\kappa_U|$. Thus, in our present formulation, the aerosol capture-(mechanism sensitive) d_{p}-dependence of both G_θ and G_ϕ (see Figs. 3 & 4) is contained in the same sensitivity coefficient, κ_U. For this sensitivity coefficient we find, and employed, the additive contributions:

$$\kappa_U = \kappa_{U,0} + \kappa_{U,1} + \kappa_{U,E} + \kappa_{U,F} \tag{A.7}$$

[10] Paper I presented results for the 'total' κ_{p}, i.e., the sum of $\kappa_{\mathrm{p,icpt}}$ and $\kappa_{\mathrm{p,mob}}$, and these sensitivity coefficient values would remain valid even for $\delta > 1$ provided this icpt/mob size ratio were nearly constant—i.e. nearly $\mathrm{Kn_{mob}}$-independent. However, for δ-values over 2 we would expect an appreciable $\mathrm{Kn_{mob}}$-dependence—i.e., a significant difference between $\delta_{\mathrm{fm}} = \delta_\infty$ and $\delta_{\mathrm{c}} = \delta_0$—as indicated for the canonical particle morphologies treated in Rosner & Fernandez de la Mora (2022). In our preliminary FF-performance data treatment (Section 4.1) we estimated a nominal ('best-fit') value of δ of ca. 2.2 for the range of $\mathrm{Kn_{mob}}$-values straddling 0.5. To further support our provisional 'simple explanation' of the Kang et al. (2019) filter capture fraction data in the "interception" domain, further information will clearly be needed about the particle shapes actually associated with KCl(s) particles with mobility diameters near, say, 300 nm. Increased attention to 'quasi-spherical' particle shape effects on capture by 'interception' would appear to be timely, especially when dealing with aerosol sources capable of producing mixtures of particle morphologies.

[11] An interesting and general new feature has been introduced by our present finding (Section 4.1) that, depending upon the aerosol source, the particles being captured may exhibit effective interception diameters significantly larger than their reported mobility diameters (see, also, Rosner & Fernandez de la Mora (2022)). Under such conditions one will clearly have to distinguish between the sensitivity coefficients κ_{p} pertaining to each of the mechanisms of interception and Brownian diffusion.

given by

$$\kappa_{U,0} = \frac{1}{3}\left(\frac{C(\mathrm{Re})}{2} - 2\right) \tag{A.8}$$

$$\kappa_{U,1} = \frac{1}{3}\left(\frac{C(\mathrm{Re})}{2} + 1\right)\left(Z - \frac{\Pi^3}{2}\right) \tag{A.9}$$

$$\kappa_{U,E} = S\frac{E'}{E}\left(\frac{C(\mathrm{Re})}{2} + 1\right) \tag{A.10}$$

$$\kappa_{U,F} = \left\{-\frac{5}{9}m\,(1-m)\ln\left(\frac{F_0}{F_\infty}\right) + S\left[m\frac{F_0'}{F_0} + (1-m)\,\frac{F_\infty'}{F_\infty}\right]\right\}\left(\frac{C(\mathrm{Re})}{2} + 1\right) \tag{A.11}$$

These relations were employed in the illustrative FF-performance calculations reported in Sections 4 and 5 above, each of which involved the d_p-dependent FF structural correction factors G_f, G_θ and G_ϕ in accord with our generalized aerosol PBE, Eq. (22) of Section 3.3.

Our present estimates of these functions of particle diameter (and their triple product) are displayed in the semi-log plot, Fig. 3 in the KCl particle size range covered in the experiments of Kang et al. (2019)—i.e., between ca. 600 nm and 20 nm. The small d_p asymptote which shows up in the plotted correction functions G_f, G_θ and G_ϕ (Figs. 3a, b, c) follows immediately from the leading term in the relevant sensitivity coefficient. While filter performance in the particle size range below 20 nm is also of considerable interest, our present approach explicitly requires $\mathrm{Pe}^{1/3} \gg 1$—a condition no longer satisfied much below $d_\mathrm{p} = 20$ nm.

The role of these filter *microstructure corrections* in altering the predictions of Paper I (for fibrous filter HF-0012 above $d_\mathrm{p} = 20$ nm) is displayed in Fig. 4, which also includes the associated experimental filter performance data reported in Kang et al. (2019). These comparisons are discussed further in Section 5, along with generalizations currently under development that will be required to self-consistently deal with the data of Kim et al. (2007) in the (Ag-np) diameter range: 20–3nm (Rosner et al. (2022)).